Quantitative FIB/SEM three-dimensional characterization of a unique Ni_4Ti_3 network in a porous Ni50.8Ti49.2 alloy undergoing a two-step martensitic transformation

Quantitative FIB/SEM three-dimensional characterization of a unique Ni_4Ti_3 network in a porous $Ni_{50.8}Ti_{49.2}$ alloy undergoing a two-step martensitic transformation

S. Cao[1], C.Y. Zeng[1], Y.Y. Li[1,2], X. Yao[3], X. Ma[1], V. Samaee[3], D. Schryvers[3], X.P. Zhang[1,*]

[1] Department of Metallic Materials Science and Engineering, School of Materials Science and Engineering, South China University of Technology, Guangzhou 510640, China

[2] School of Materials Science and Engineering, Foshan University, Foshan 528225, China

[3] EMAT, University of Antwerp, Groenenborgerlaan 171, B-2020 Antwerp, Belgium

*Corresponding author: mexzhang@scut.edu.cn

Abstract

The three-dimensional (3D) nanostructure of Ni_4Ti_3 precipitates in a porous $Ni_{50.8}Ti_{49.2}$ alloy has been reconstructed by "Slice-and-View" in a Focused Ion Beam/Scanning Electron Microscope (FIB/SEM). The 3D configuration of these precipitates forming a network structure in the B2 austenite matrix has been characterized via 3D visualization and quantitative analysis including volume fraction, skeleton, degree of anisotropy and local thickness. It is found that dense Ni_4Ti_3 precipitates occupy 54% of the volume in the B2 austenite matrix. Parallel Ni_4Ti_3 precipitates grow alongside the surface of a micro-pore, yielding an asymmetric structure, while nano-voids do not seem to affect the growth of Ni_4Ti_3 precipitates. The small average local thickness of the precipitates around 60 nm allows their coherency with the matrix, and further induces the R-phase transformation in the matrix. On the other hand, the B2 matrix exhibits a winding and narrow structure with a skeleton of 18.20 mm and a thickness similar to the precipitates. This discontinuous matrix segmented by the Ni_4Ti_3 network and pores is responsible for the gradual transformation by stalling the martensite propagation.

Key words: Porous Ni–Ti shape memory alloy, Ni_4Ti_3 precipitate, FIB/SEM, Three-dimensional reconstruction, Martensitic transformation

1. Introduction

Porous Ni–Ti shape memory alloys (SMAs) have been widely investigated as promising materials for use in biomedical implants and devices, dampers, and hydrogen isotope separators, due to their excellent mechanical properties, bio-compatibility, low density and unique pore structure [1]. Moreover, similar to dense Ni–Ti alloys, the porous ones also exhibit unique shape memory effect and superelasticity originating from the martensitic transformation in the alloys, allowing them to be good candidates for light-weight actuators [1, 2].

Ni_4Ti_3 precipitates of rhombohedral structure have drawn considerable attention due to their contribution to the B2–B19′ martensitic transformation and transformation-related functional properties of Ni–Ti binary SMAs [3, 4]. These lenticule-shaped precipitates can appear in four orientation variants with a central plane perpendicular to one of the $<111>_{B2}$ directions [5, 6]. The strain field induced by coherent or semi-coherent Ni_4Ti_3 precipitates smaller than 300 nm in the surrounding B2 matrix favors an intermediate R–phase transformation, whereas the slightly higher Ni fraction in the precipitates leads to Ni depletion in the matrix, yielding an upward shift of martensitic transformation temperatures. Normally, the nucleation and growth of these precipitates,

controlled by a diffusion process, are strongly dependent on the composition and thermal-mechanical treatments of the alloy, which finally determine the size, morphology and distribution of the precipitates. In the past decades, systematic studies have been carried out on various Ni_4Ti_3 precipitation behaviors and their influence on the martensitic transformation in different types of dense Ni–Ti alloys after different thermal-mechanical histories. These mainly include Ni_4Ti_3 precipitates of selective variants in single crystal and polycrystalline $Ni_{51}Ti_{49}$ alloys after stress-assistant aging [7–11], autocatalytically grown Ni_4Ti_3 precipitates in a stress-free aged $Ni_{51}Ti_{49}$ single crystal [12], heterogeneous precipitation in a polycrystalline $Ni_{50.8}Ti_{49.2}$ alloy with multi-stage martensitic transformation [13–16], ultra-fine precipitates and even Ni clusters induced by low temperature aging [17–19]. In contrast, for the porous Ni–Ti alloys, most investigations have been focused on fabrication, mechanical property optimization and surface modification of the alloys [20–27], and there have been very limited studies concerning the Ni_4Ti_3 precipitates in porous alloys [28, 29]. The unique precipitation behavior of Ni_4Ti_3 under the influence of a discontinuous matrix and their contribution to the martensitic transformation of porous NiTi alloys are still in need of a comprehensive study.

The Focused Ion Beam/Scanning Electron Microscope (FIB/SEM) dual-beam system allows serial cross-sectioning and imaging with resolution down to the nanoscale. With the help of the so-called “Slice-and-View” procedure, a sequence of two-dimensional (2D) cross-section images can be acquired automatically for three-dimensional (3D) reconstruction. It has been validated in former studies that FIB/SEM is a proper candidate to reveal the 3D morphology and distribution of micron or sub-micron Ni_4Ti_3 precipitate particles in dense Ni–Ti alloys [9, 12, 16]. In the present study, the 3D configuration of Ni_4Ti_3 precipitates in a porous $Ni_{50.8}Ti_{49.2}$ alloy after mid-term aging is investigated via the FIB/SEM dual-beam system. Quantitative analysis of the Ni_4Ti_3 configuration based on the reconstructed 3D volume is conducted to reveal the effect of the pore structure on the unique precipitation behavior. The influence of the Ni_4Ti_3 configuration on the martensitic transformation behavior of the porous $Ni_{50.8}Ti_{49.2}$ alloy and the propagation of martensite during phase transformation are also discussed.

2. Experiments

2.1 Preparation of the porous $Ni_{50.8}Ti_{49.2}$ alloy and sample for microanalysis

A porous $Ni_{50.8}Ti_{49.2}$ alloy was produced via gradient powder sintering [24]. First, nickel and titanium powders (60 μm and 50 μm, respectively, 99.9% purity) with a nominal atomic ratio of 50.8:49.2 were blended for 24 h. Then, the homogenous mixture was blended with 10% weight fraction NH_4HCO_3 particles (150–200 μm, 99.99% purity), which acted as space holder for 8 h, followed by cold compact in a hydraulic presser at 100 MPa. The cylinder-shaped green sample (16×15, diameter × height, mm) was heated up gradually to 1273 K and sintered for 3 h under a protective atmosphere of flowing argon gas (99.99%). Finally, the as-sintered sample was solution treated at 1273 K for 10 h and then subjected to aging at 773 K for 6 h. Both heat treatments were carried out in evacuated quartz tubes and followed by water quenching. The phase transformation behavior of the as-obtained porous alloy was analyzed by differential scanning calorimetry (DSC, Q200, TA) with both cooling and heating rates of 5 K/min in temperature ranges of 243–313 K and 193–353 K, respectively, which allow different partial transformation tests. Phase constituents of the porous alloy were characterized by X-ray diffraction (XRD, Philips X'pert) with Cu-Kα radiation at a scanning step of 0.02°. Ni_4Ti_3 was identified by (scanning) transmission electron

microscopy ((S)TEM, Orisis, FEI). The TEM sample preparation and 3D pore structure characterization were carried out in a FIB/SEM dual-beam system (Helios Nanolab 650, FEI).

2.2 Image acquisition and processing

The acquisition of the 2D image sequence for Ni_4Ti_3 3D reconstruction was conducted via the "Slice-and-View" procedure in FIB/SEM under optimized slicing and imaging conditions, which were needed due to the weak contrast of the Ni_4Ti_3 precipitates with similar composition and structure to the surrounding matrix [30, 31]. In the present study, 200 cross-section images with an interval of 20 nm at a selected area close to a pore in the sample were collected. The image sequence was firstly well aligned in Amira©, and then resized to compensate image distortions before selection of interesting regions in ImageJ© [30, 31]. The image quality of the as-obtained 2D image sequence needs to be improved before image segmentation to allow 3D reconstruction and quantitative analysis of high precision. A sequence of filters in ImageJ© and MatLab© was applied to remove the so-called "curtain" artifacts introduced by a low dose FIB milling and heterogeneous sample hardness [32], decreasing noise, enhancing contrast and subtracting the gradient background [16]. Afterwards, the processed image sequence was binarized and labeled in Amira© to allow separate segmentation of Ni_4Ti_3 precipitates and the B2 matrix, excluding the pore region. Finally, the 3D visualization is achieved by the surfacegen function through the segmented sequence of cross-section images in Amira©.

2.3 Quantitative data extraction

Quantitative analysis was performed to acquire characteristic structural parameters for a detailed description of the 3D configuration of Ni_4Ti_3 precipitates in the as-segmented matrix in the reconstructed bulk. Since the pixel size in the imaging plane is different from that along the slicing direction, it is necessary to resample the 3D data set to an isotropic voxel size before quantitative analysis. In this study, the 3D data set was resampled along the slicing direction by a B-spline interpolation method in Amira©, leading to an isotropic voxel size of 4 nm × 4 nm × 4 nm.

The volume fraction of Ni_4Ti_3 precipitates can easily be calculated by voxel counting based on the segmented 3D volume. A "skeletonization" process was carried out in the B2 matrix via Amira© with the so-called "distance-ordered homotopic thinning algorithm" [33, 34]. In this way, the centerline of interconnected regions can be extracted from the 3D image data, which reveals the propagation path of martensite during phase transformation.

The so-called "degree of anisotropy" (DA) as an indicator to detect structural alignments along certain direction, was introduced to quantitatively describe the symmetry state of the reconstructed 3D volume (DA = 0 = maximum isotropy; DA = 1 = maximum anisotropy). In Amira©, DA is acquired by the mean intercept length (MIL) method and eigenvalue analysis. MIL analysis allows the measurement of structural isotropy by acquiring the differences in the frequency with which a set of oriented rays encounter a 3D object in different directions [35, 36]. The mean number of intersect as a function of angle with a fixed interval of 10 degree forms the data cloud then used in eigenvalue analyses. Both the minimal and maximal eigenvalues can be extracted from this analysis, by which DA is defined as:

$$DA=1-\frac{\mathrm{Min}_{eigenvalue}}{Max_{eigenvalue}} \quad (1)$$

As a result, DA varies from 0 to 1, with the former standing for absolute isotropy and the latter

for absolute anisotropy.

An in-depth investigation of local configurations of both Ni_4Ti_3 precipitates and the as-segmented matrix was conducted by the "local thickness" function in ImageJ©. Local thickness of an object is defined by the diameter of the maximal sphere at every point which completely fits inside the structure with the corresponding point included [37]. This parameter is used to reveal the local structural characteristics of objects with irregular shape. In this study, the volume-based local thickness was computed to quantify the thickness and interspace of Ni_4Ti_3 precipitates.

3. Results and discussion

3.1 Microstructure and phase transformation of the porous $Ni_{50.8}Ti_{49.2}$ alloy

A top-view of the as-received porous $Ni_{50.8}Ti_{49.2}$ alloy using secondary electron (SE) imaging is shown in Fig.1(a). Both large pores around 200 μm introduced by the space holder and smaller ones around 50 μm inherited from the raw particle size with irregular shape can be observed in the porous alloy. According to the XRD pattern in Fig. 1(b), this porous alloy mainly consists of austenite NiTi (B2 phase), together with secondary phases of Ni_4Ti_3, $Ti_4Ni_2(O,C)$ and Ni_3Ti. $Ti_4Ni_2(O,C)$ is the oxycarbide of intermetallic Ti_2Ni, and the latter is typically introduced by solid state diffusion between Ni and Ti, together with Ni_3Ti [38].

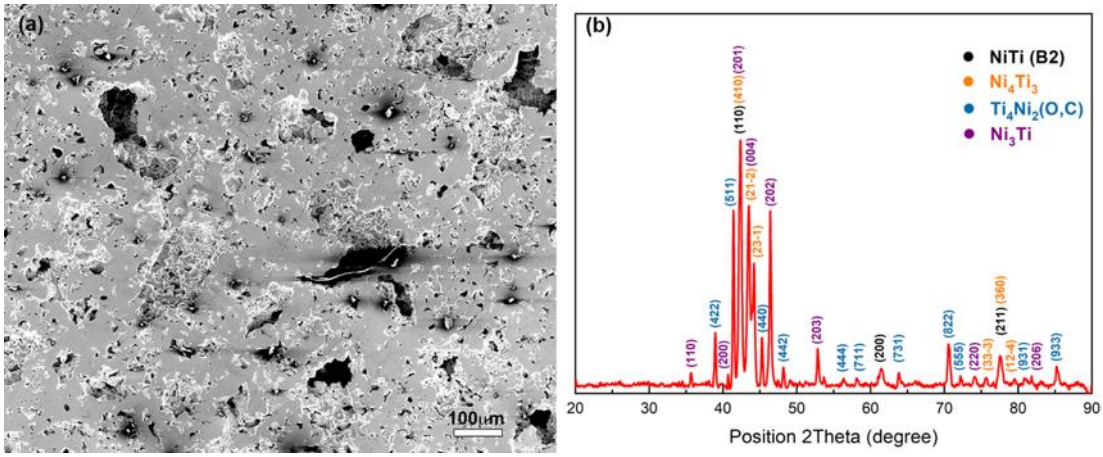

Fig. 1. Top-view SE image (a) and XRD pattern (b) of the $Ni_{50.8}Ti_{49.2}$ porous alloy

Fig. 2(a) presents a high-angle annular dark field (HAADF)-STEM image from a cross-section sample obtained in the vicinity of a pore. Different variants of lenticule-shaped precipitates with a dense distribution can be seen. The reflections at 1/7 $<-321>_{B2}$ positions in the corresponding selective area electron diffraction (SAED) pattern along the $[111]_{B2}$ zone shown in Fig. 2(b) indicate that these precipitates are rhombohedral Ni_4Ti_3, with $[111]_{R\text{-}Ni4Ti3}$ parallel to $[111]_{B2}$.

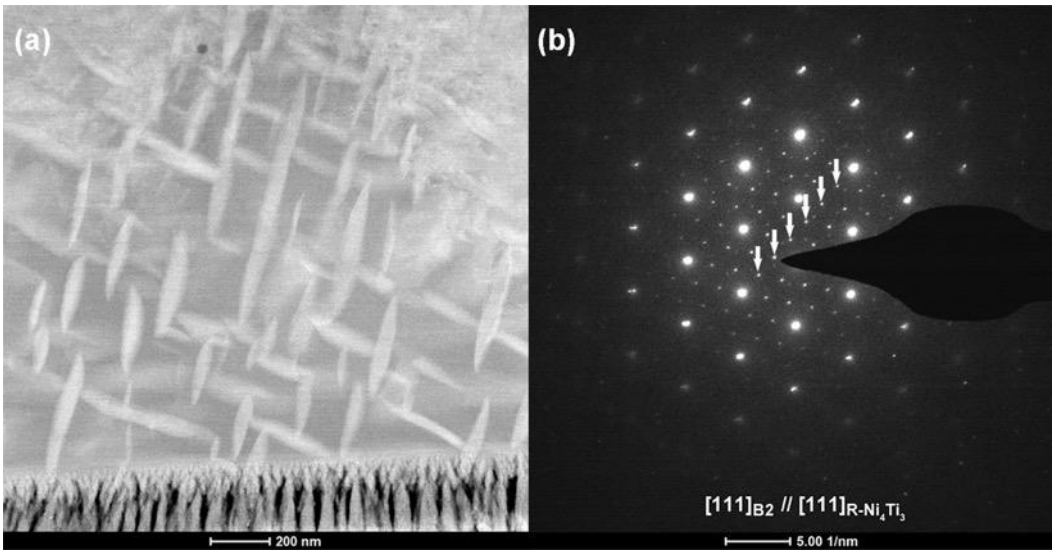

Fig. 2. HAADF-STEM image showing (a) lenticular Ni_4Ti_3 precipitates and corresponding SAED pattern (b) of a cross-section sample obtained in the vicinity of a pore in the porous $Ni_{50.8}Ti_{49.2}$ alloy, in which the reflections at 1/7 $<-321>_{B2}$ positions are characteristic spots of Ni_4Ti_3 and are marked by arrows in (b)

One of the original cross-section images obtained by "Slice-and- View" and the corresponding segmented image for 3D reconstruction are exhibited in Fig. 3(a) and (b), respectively. It can be observed that slightly bright lenticule-shaped Ni_4Ti_3 precipitates similar to those shown in Fig. 2(a) with a length varying from ~150 nm to 2 μm lying atop a pore region show obvious orientation preference in the gray B2 matrix. Notably, this orientation preference is somehow interrupted by the presence of the crack in the matrix, as indicated in Fig. 3(b). The pore is bordered by bright blocky-shaped Ni_3Ti and dark $Ti_4Ni_2(O,C)$ particles, whose existence is confirmed by the XRD pattern shown in Fig.1(b).

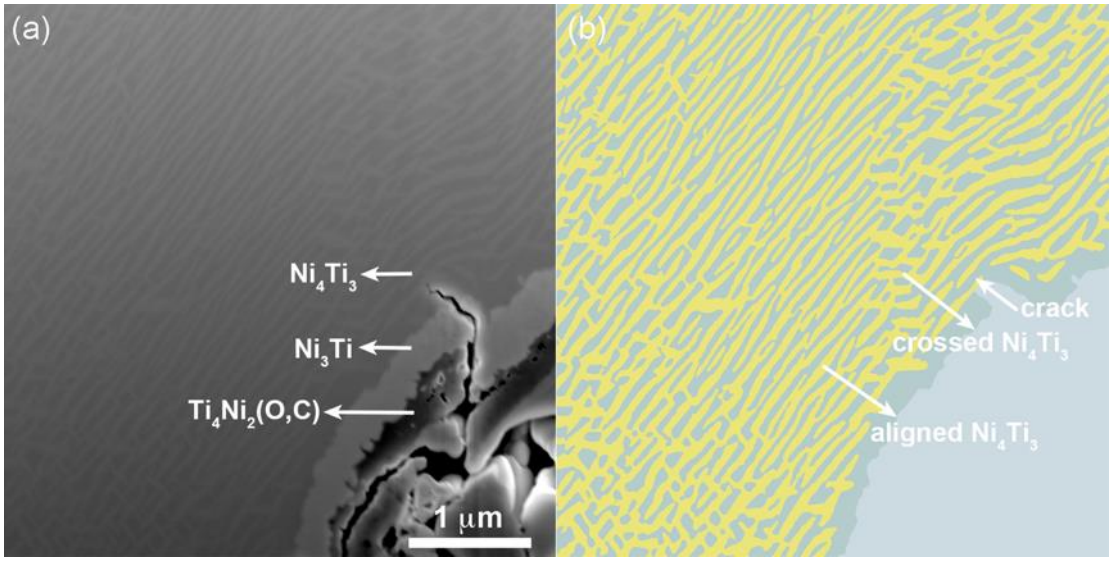

Fig. 3. One of the 2D cross-section SEM images of the porous $Ni_{50.8}Ti_{49.2}$ alloy (a) and the corresponding segmented image after labelling (b), with yellow indicating Ni_4Ti_3 precipitates and pea green standing for the matrix.

According to DSC curves shown in Fig. 4, a single step transformation occurs in the porous $Ni_{50.8}Ti_{49.2}$ alloy upon cooling to 243 K. The narrow hysteresis between the forward and reverse transformations suggests a B2–R transformation upon cooling, which is followed by the R–B19′ transformation with a much larger hysteresis when further cooling to 193K. The corresponding phase transformation temperatures, with the starting and finishing temperatures of the R-phase and martensite denoted by R_s, R_f, M_s and M_f, and likewise the starting and finishing temperatures of the inverse martensite and austenite represented by M_s', M_f', A_s and A_f, respectively, are listed in Table 1.

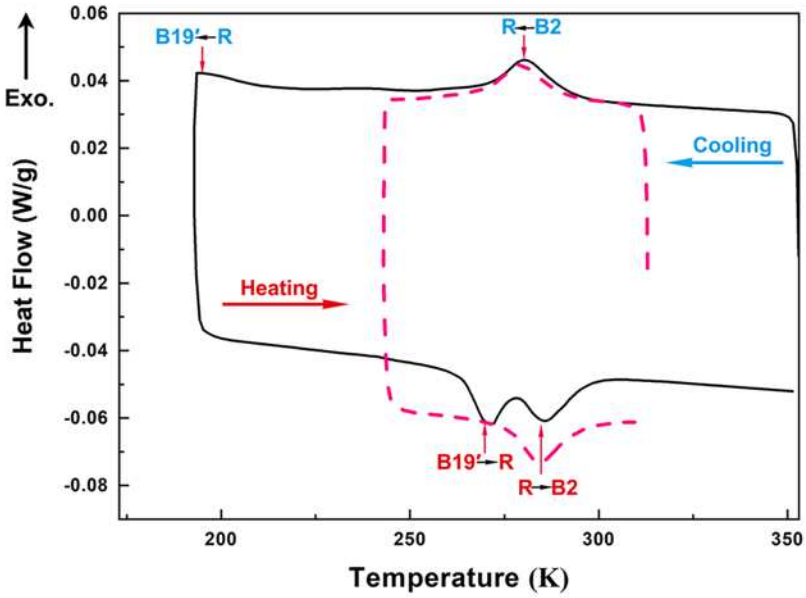

Fig. 4. DSC curves of the porous $Ni_{50.8}Ti_{49.2}$ alloy in temperature ranges of 243–313 K (red dashed-line) and 193–353 K (dark solid-line).

Table 1. Phase transformation temperatures of the porous $Ni_{50.8}Ti_{49.2}$ alloy

R_s (K)	R_f (K)	M_s (K)	M_f (K)	M_s' (K)	M_f' (K)	A_s (K)	A_f (K)
294	270	211	–	263	275	280	297

3.2 Effect of the pore and nano-void on Ni_4Ti_3 precipitation

A 3D volume of 4.50 μm × 4.50 μm × 4.00 μm was reconstructed through the segmented sequence of cross-section images. According to the reconstructed 3D visualization shown in Fig. 5(a), dense Ni_4Ti_3 precipitates (yellow) coalesce into a cross-linked 3D network in the matrix (blue) of the reconstructed volume, rather than grow out to individual particles as in most known cases. Regions with parallel Ni_4Ti_3 precipitates of preferred orientation (A) and crossed ones of different variants (B) can be observed in Fig. 5(b) and (c), respectively (and where the precipitates now show up as whitish shapes). Moreover, pores and voids of different scales clearly play different roles in the Ni_4Ti_3 growth. When zooming in on the reconstructed region, parallel precipitates with their central planes alongside and following the surface of a micro-sized pore can be found in Fig. 6(a). Clearly, some of these are even bent to accommodate to the curved pore wall. This can be understood by the fact that the concentrated residual stress around the pore from sample preparation acts as compression in the material during aging, leading to preferentially oriented Ni_4Ti_3 precipitates

perpendicular to the stress direction indicated by purple arrows shown in Fig. 6(a). A similar effect of micro-scaled pores in the powder-sintered porous $Ni_{50.8}Ti_{49.2}$ alloy on the preferred orientation of Ni_4Ti_3 was also reported in our former TEM study [28]. Noteworthy, since the pores in the porous alloy normally have irregular shape, the stress field induced by the pores in the matrix could be inhomogeneous. Particularly, when a crack propagates from the pore region into the matrix, the particular stress field surrounding the crack may interrupt the preferred orientation of Ni_4Ti_3, and thus break the alignment of the precipitates, as shown in Fig. 3(b) and Fig. 5(a). Compared to the micro-scaled pores, the nano-sized voids hardly have any influence on the distribution and orientation of the precipitates, as can be concluded from Fig. 6(b), where the shape and direction of a nearby precipitate remain the same in the presence of a nano-void. This implies a very weak stress field surrounding the void and insufficient to interfere with the growth of Ni_4Ti_3.

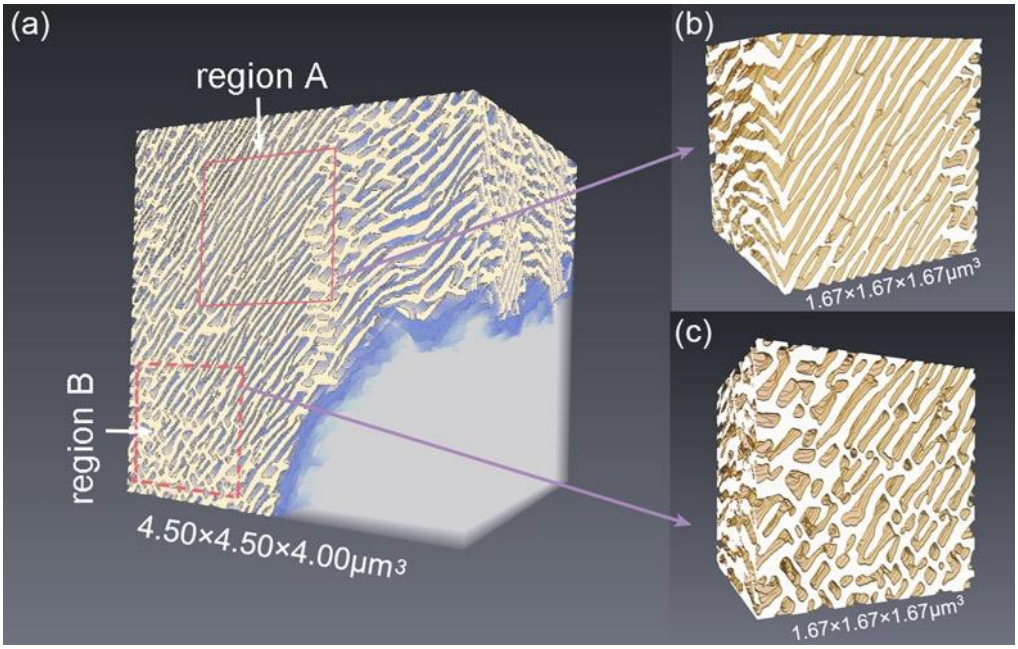

Fig. 5. 3D reconstructed volume of the porous $Ni_{50.8}Ti_{49.2}$ alloy (a) with parallel Ni_4Ti_3 precipitates of preferred orientation in region A (b) and crossed ones of different variants in region B (c).

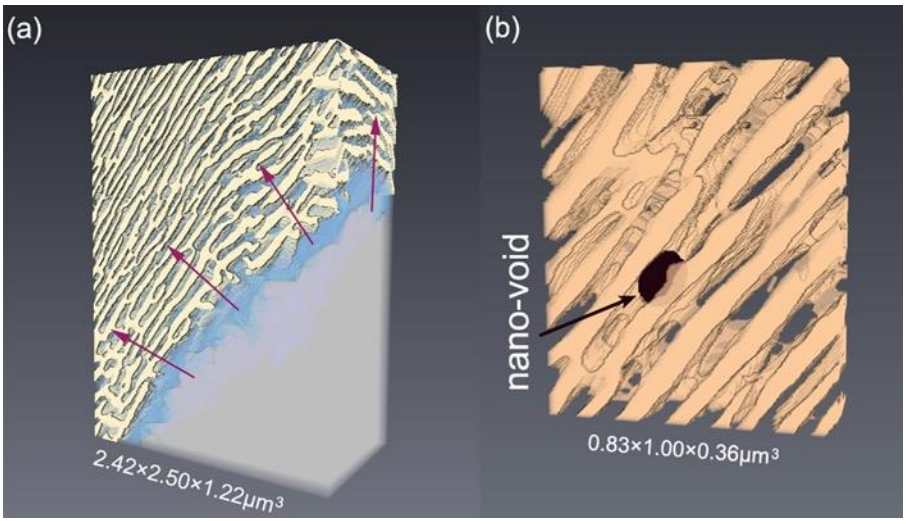

Fig. 6. Parallel precipitates around a micro-sized pore with their central planes following the edge of the pore (a) and unaltered growth of Ni_4Ti_3 precipitates around a nano-void (b).

3.3 Global structural analysis

Overall and based on voxel counting it was found that the precipitates occupy 46% of the space in the entire reconstructed region and 54% in the B2 matrix (i.e., without counting the pore region). This very high volume ratio and such a dense arrangement of Ni_4Ti_3 precipitates can be attributed to the occurrence of a large number of point defects in porous alloys produced via powder metallurgy, which act as nuclei for precipitation. Meanwhile, due to the presence of other secondary particles, the local composition of the matrix can be much more Ni-rich than the nominal composition, thus leading to a sufficient supersaturation of Ni to allow a large amount of Ni_4Ti_3 precipitation. Indeed, considering the M_s of 211 K, according to calculation by Tang et al [39], the matrix composition is around $Ni_{50.6}Ti_{49.4}$, based on which a matrix composition of $Ni_{54.1}Ti_{45.9}$ before Ni_4Ti_3 precipitation can be estimated. Given the occurrence of large amounts of $Ti_4Ni_2(O,C)$ and Ni_3Ti precipitates, as indicated in Fig. 1(b) and Fig. 3(a), such a shift from the nominal composition is indeed possible. Unfortunately, scans of sufficiently large regions to cover statistical amounts of such precipitates to confirm this concentration balance could not be obtained.

Ni_4Ti_3 precipitates with such a unique 3D structure segment the matrix into a similar network. The 3D matrix (yellow) and the as-extracted skeleton (purple) are shown in Fig. 7, where both of them show a tortuous geometry. Moreover, the total length of the matrix skeleton reaches 18.20 mm, which is more than 4000 times the side length of the reconstructed volume. This geometry implies a long winding path for martensite to propagate during phase transformation.

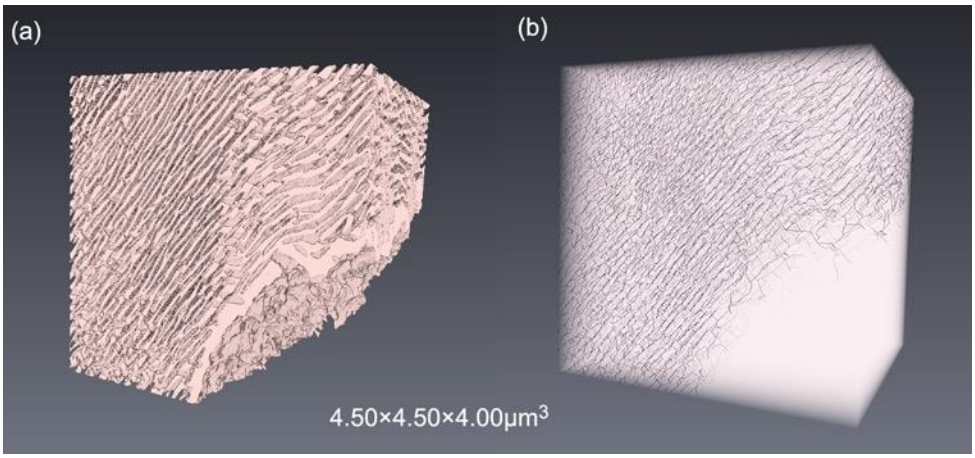

Fig. 7. 3D view of the B2 matrix (light pink) of the reconstructed region (a) and its skeleton (purple) (b)

3.4 Local structural analysis

Since the coalescent Ni_4Ti_3 precipitates form a cross-linked 3D network, parameters like volume, specific surface area, aspect ratio, sphericity and Feret diameters used to describe the size and morphology of an individual particle are no longer adaptable to the present case, whereas local structural parameters delivering information on the size and symmetry state of networks are more relevant to describe the 3D configuration. In the present study, the local structure of the Ni_4Ti_3 network was further quantified via a comparison study between region A with parallel precipitates and region B with crossed precipitates, as shown in Fig. 5.

Based on the 3D symmetry analysis, DA is calculated as 0.58 in region A and 0.50 in region B, the latter being close to that in the grain interior of bulk polycrystal $Ni_{50.8}Ti_{49.2}$ with multiple variants

reported in a previous study [16]. This obvious but not yet significant difference in symmetry can easily be explained by the different orientations and distributions of Ni_4Ti_3 in the two regions. Due to the 3D anisotropic morphology and fixed orientation relationship with the B2 matrix, the as-grown Ni_4Ti_3 precipitates can never approach absolute isotropy with a DA close to 0, no matter how many variants present, such as in region B. Furthermore, when the precipitates of a single variant are well aligned, the isotropy is thus lowered with increasing DA, such as in region A. This thus also implies that the matrix in region A is segmented into spaces with lower symmetry by the parallel precipitates than is the case in region B.

Figs. 8 and 9 present 3D local thickness maps and distribution diagrams of Ni_4Ti_3 precipitates and the matrix in both region A and region B, respectively. The matrix in region A is mostly segmented by parallel precipitates into lamella-shaped volumes with preferential orientation, according to Fig. 8. In contrast, the matrix in region B is segmented by Ni_4Ti_3 precipitates of different orientations into volumes of different morphologies. Both rod-like volumes induced by crossed Ni_4Ti_3 precipitates and lamella-shaped ones separated by parallel precipitates can be observed, as shown in Fig. 9. Moreover, the former normally yield larger local thickness according to the thickness map presented in Fig. 9(b). Distribution histograms in Figs. 8 and 9 indicate that the local thicknesses of Ni_4Ti_3 precipitates and the matrix in both regions closely follow a normal distribution. Numeric data extracted from the local thickness maps in Figs. 8 and 9 are given in Table 2. One should note that the calculated minimum local thickness of 8 nm for both Ni_4Ti_3 precipitates and the matrix in both regions is limited by the voxel size of 4 nm × 4 nm × 4 nm in the reconstructed volume, but since this only affects the left extremity of the curve, it is not expected to imply any strong impact on the numbers. Based on the distribution histograms and the numeric data, 68% of Ni_4Ti_3 precipitates in region A have a local thickness in the range of 41–69 nm, while this range lies between 35–63 nm for the matrix in the same region. On the other hand, in region B, this average domain of the precipitates falls in the range of 50–90 nm, whilst it is 42–80 nm for the corresponding matrix. These results together with the numeric data shown in Table 2 indicate small thickness and narrow interspace of Ni_4Ti_3 precipitates in both regions. Moreover, the thickness of the precipitates and their corresponding interspaces fall within the similar range with very close averages. The interspace of the precipitates shows a positive correlation with their thickness, meaning that the thicker the precipitates, the wider the matrix interspace in between them. The larger average and maximum local thicknesses of the precipitates and the as-segmented matrix in region B can be attributed to the crossed precipitates of different variants, which can also explain the larger spread of the data in region B can also be interpreted this way. Indeed, the coalescence of precipitates on the one hand thicken themselves at the intersections, on the other hand, these intersections further lead to interspace of rod-like volume with a relatively larger thickness than the lamella-shaped ones, according to the local thickness map shown in Fig. 9. These quantitative results confirm the ultra-fine structure of the Ni_4Ti_3 network. Despite of the high volume fraction and coalescence, instead of coarsening, the Ni_4Ti_3 precipitates remain thin and segment the matrix into narrow volumes of comparable thickness.

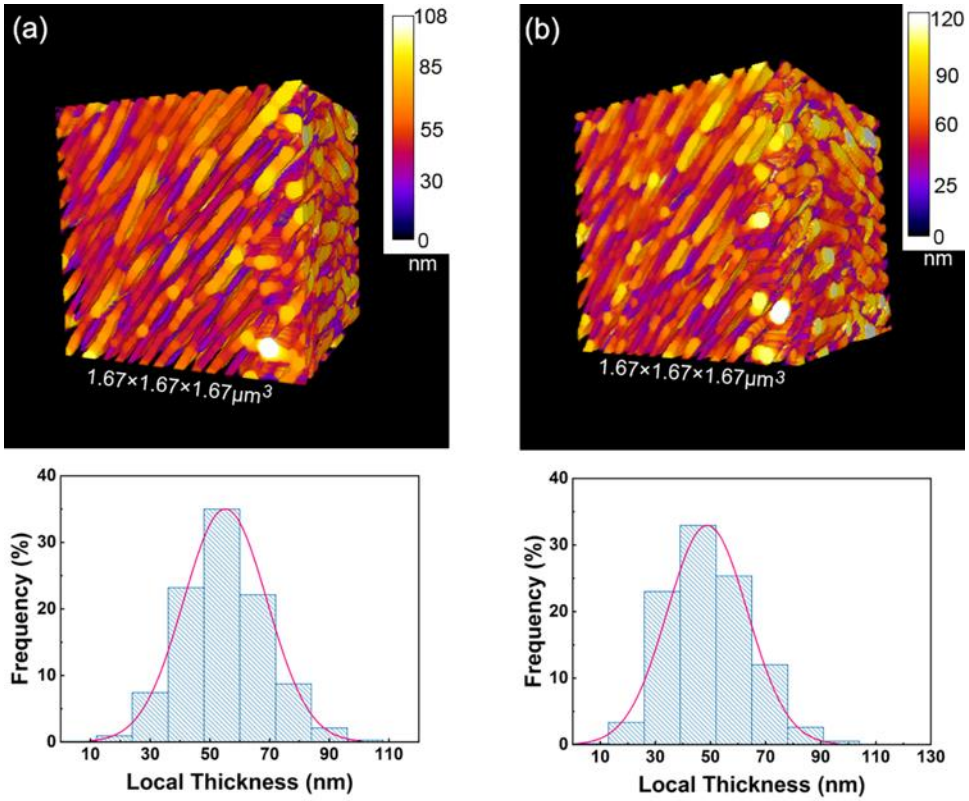

Fig. 8. 3D local thickness maps and corresponding distribution histograms of Ni_4Ti_3 precipitates (a) and matrix (b) in region A.

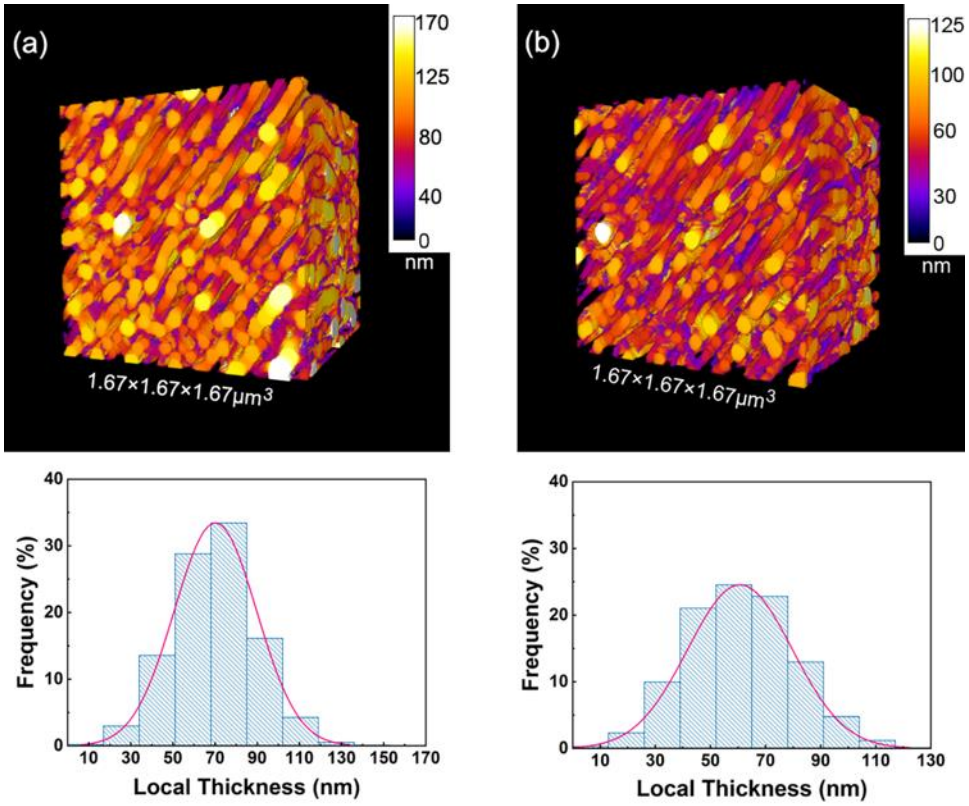

Fig. 9. 3D local thickness maps and corresponding distribution histograms of Ni_4Ti_3 precipitates (a) and matrix (b) in region B.

Table 2. Numeric data of local thickness of the Ni_4Ti_3 precipitates and matrix in regions A and B

	Minimum (nm)	Maximum (nm)	Average (nm)	Standard deviation (nm)
Ni_4Ti_3 - Region A	8	122	55	14
Matrix - Region A	8	120	49	14
Ni_4Ti_3 - Region B	8	169	70	20
Matrix - Region B	8	125	61	19

3.5 3D configuration of Ni_4Ti_3 and phase transformation behavior

The occurrence of R-phase transformation confirmed by DSC shown in Fig. 4 implies the existence of coherent stress field induced by the Ni_4Ti_3 network, even though its characteristic length scale far exceeds the critical length of ~300 nm for such precipitates to retain coherency with the matrix [40, 41]. This can be attributed to small local thicknesses of both the precipitates and as-segmented matrix. The lattice mismatch between the B2 matrix and Ni_4Ti_3 precipitates has a much larger value along the normal of the central plane (thickness direction) than in the directions parallel with the central plane (length direction) (which at the same time explains their shape) [5]. Therefore, despite the limited increase in thickness during coarsening of classic precipitates in bulk material, the accumulation of the lattice mismatch in the thickness direction enhances the surrounding strain field significantly and finally introduces misfit dislocations to release the coherency strain. In the case of the Ni_4Ti_3 network, however, the thickness of the network remains small, and the coalescence of precipitates leads to a length much larger than that of individual Ni_4Ti_3 precipitates with the same thickness. Indeed, the average local thicknesses of precipitates in regions A and B, i.e., 55±14 nm and 70±20 nm respectively, match well with the average thickness of 68.5 nm for individual coherent Ni_4Ti_3 particles in a $Ni_{50.8}Ti_{49.2}$ polycrystal, whose average length is only 304 nm, just around the critical length of individual precipitates to retain coherency or semi-coherency [16]. Consequently, thickness rather than length becomes a more critical factor for the coherency in the network case. Moreover, much less ending sharp edges, on which lattice distortion of the matrix can also be found, exist in the network due to the coalescence when compared with individual precipitates [42]. In this way, a relatively small thickness is sufficient for allowing coherency of the Ni_4Ti_3 network regardless of its length. Meanwhile, since the matrix in regions A and B has been segmented into narrow channels of 49–61 nm in average, the coherent strain field induced by the Ni_4Ti_3 network can almost cover the entire matrix [42, 43] and thus lead to an obvious B2–R transformation peak in the DSC curves. Moreover, the parallel precipitates of higher DA in region A induce a coherent stress field of preferential orientation, and further lead to R and B19′ phases of selective variants upon cooling [28]. Unlike the typical B2–R transformation with a narrow exothermic peak in dense Ni–Ti alloys, wide peaks of both B2–R and R–B19′ transformations can be found in the porous alloy. On the one hand, these wide peaks can be attributed to the long and winding space segmented by the Ni_4Ti_3 network and affecting the propagation of R and B19′ during the transformation [8]. On the other hand, the discontinuous matrix segmented by the pores is also responsible for stalling the martensite propagation during the transformation and thus yielding a gradual transformation process [44]. Also, the large variation in nucleation sites at the matrix/precipitate interface affected by neighboring strain fields can cause a spread in the onset of nucleation.

4. Conclusions

In the present study, the FIB/SEM dual-beam system was employed to characterize the 3D configuration of Ni_4Ti_3 precipitates forming a network structure in the B2 matrix of a porous $Ni_{50.8}Ti_{49.2}$ alloy by means of the "Slice-and-View" procedure. The conclusions obtained from 3D reconstruction and quantitative studies are summarized as follows:

(1) Highly dense Ni_4Ti_3 precipitates in the porous $Ni_{50.8}Ti_{49.2}$ alloy treated by mid-term aging coalesce into a 3D network, leading to a volume fraction of 54% in the B2 matrix.

(2) Nano-scaled voids in the matrix show little influence on the precipitation of Ni_4Ti_3, while micro-scaled pores with concentrated residual stress lead to preferred orientation of Ni_4Ti_3. This asymmetric configuration of precipitates confirmed by a degree of anisotropy (DA) of 0.58 may confine the martensite variants during phase transformation.

(3) Ni_4Ti_3 network with a small thickness around 60 nm retain the coherency with the B2 matrix, allowing occurrence of the R–phase transformation. The B2 matrix is segmented by the precipitates into long and narrow space with a skeleton of 18.20 mm and a comparable thickness to the precipitates. This discontinuous and winding structure of the matrix induced by Ni_4Ti_3 network and pores stalls the martensite propagation during the transformation and thus yields a gradual transformation process.

Acknowledgements

This work was supported by the National Natural Science Foundation of China under Grant Nos. 51401081 and 51571092, the Natural Science Foundation of Guangdong Province through Key Project under Grant No. 2018B0303110012 and General Project under Grant No. 2017A030313323, and China Scholarship Council (CSC).

Data availability

The raw/processed data required to reproduce these findings cannot be shared at this time as the data also forms part of an ongoing study.

References

[1] V. Antonucci, A. Martone, Chapter 2 - Phenomenology of Shape Memory Alloys, in: L. Lecce, A. Concilio (Eds.), Shape Memory Alloy Engineering, Butterworth-Heinemann, Boston, 2015, pp. 33–56.

[2] K. Otsuka, X. Ren, Physical metallurgy of Ti–Ni-based shape memory alloys, Progress in Materials Science 50(5) (2005) 511–678.

[3] S. Miyazaki, K. Otsuka, Deformation and transition behavior associated with the R-phase in Ti-Ni alloys, Metallurgical Transactions A 17(1) (1986) 53–63.

[4] J. Frenzel, E.P. George, A. Dlouhy, C. Somsen, M.F.X. Wagner, G. Eggeler, Influence of Ni on martensitic phase transformations in NiTi shape memory alloys, Acta Materialia 58(9) (2010) 3444–3458.

[5] T. Tadaki, Y. Nakata, K. Shimizu, K. Otsuka, Crystal-Structure, Composition and morphology of a precipitate in an aged Ti-51 at percent-Ni shape memory alloy, T Jpn I Met 27(10) (1986) 731–740.

[6] M. Nishida, C.M. Wayman, Electron microscopy studies of precipitation processes in near-equiatomic TiNi shape memory alloys, Mater Sci Eng 93 (1987) 191–203.

[7] J. Khalil-Allafi, A. Dlouhy, G. Eggeler, Ni_4Ti_3-precipitation during aging of NiTi shape memory alloys and its influence on martensitic phase transformations, Acta Materialia 50(17) (2002) 4255–4274.

[8] J. Michutta, C. Somsen, A. Yawny, A. Dlouhy, G. Eggeler, Elementary martensitic transformation processes in Ni-rich NiTi single crystals with Ni_4Ti_3 precipitates, Acta Materialia 54(13) (2006) 3525–3542.
[9] S. Cao, C. Somsen, M. Croitoru, D. Schryvers, G. Eggeler, Focused ion beam/scanning electron microscopy tomography and conventional transmission electron microscopy assessment of Ni_4Ti_3 morphology in compression-aged Ni-rich Ni–Ti single crystals, Scripta Materialia 62(6) (2010) 399–402.
[10] Y.Y. Li, S.S. Cao, X. Ma, C.B. Ke, X.P. Zhang, Influence of strongly textured microstructure on the all-round shape memory effect of rapidly solidified $Ni_{51}Ti_{49}$ alloy, Materials Science and Engineering: A 705 (2017) 273–281.
[11] A. Radi, J. Khalil-Allafi, M.R. Etminanfar, S. Pourbabak, D. Schryvers, B. Amin-Ahmadi, Influence of stress aging process on variants of nano-Ni_4Ti_3 precipitates and martensitic transformation temperatures in NiTi shape memory alloy, Materials & Design 142 (2018) 93–100.
[12] S. Cao, S. Pourbabak, D. Schryvers, Quantitative 3-D morphologic and distributional study of Ni_4Ti_3 precipitates in a $Ni_{51}Ti_{49}$ single crystal alloy, Scripta Materialia 66(9) (2012) 650–653.
[13] M. Nishida, T. Hara, T. Ohba, K. Yamaguchi, K. Tanaka, K. Yamauchi, Experimental consideration of multistage martensitic transformation and precipitation behavior in aged Ni-rich Ti-Ni shape memory alloys, Mater Trans 44(12) (2003) 2631–2636.
[14] G. Fan, W. Chen, S. Yang, J. Zhu, X. Ren, K. Otsuka, Origin of abnormal multi-stage martensitic transformation behavior in aged Ni-rich Ti–Ni shape memory alloys, Acta Materialia 52(14) (2004) 4351–4362.
[15] K. Fujishima, M. Nishida, Y. Morizono, K. Yamaguchi, K. Ishiuchi, T. Yamamuro, Effect of heat treatment atmosphere on the multistage martensitic transformation in aged Ni-rich Ti–Ni alloys, Materials Science and Engineering: A 438-440 (2006) 489–494.
[16] S. Cao, M. Nishida, D. Schryvers, Quantitative three-dimensional analysis of Ni_4Ti_3 precipitate morphology and distribution in polycrystalline Ni–Ti, Acta Materialia 59(4) (2011) 1780–1789.
[17] J. Kim, S. Miyazaki, Effect of nano-scaled precipitates on shape memory behavior of Ti-50.9at.%Ni alloy, Acta Materialia 53(17) (2005) 4545–4554.
[18] X. Wang, S. Kustov, K. Li, D. Schryvers, B. Verlinden, J. Van Humbeeck, Effect of nanoprecipitates on the transformation behavior and functional properties of a Ti–50.8 at.% Ni alloy with micron-sized grains, Acta Materialia 82 (2015) 224–233.
[19] S. Pourbabak, X. Wang, D. Van Dyck, B. Verlinden, D. Schryvers, Ni cluster formation in low temperature annealed $Ni_{50.6}Ti_{49.4}$, Functional Materials Letters 10(01) (2017) 1740005.
[20] J.S. Kim, J.H. Kang, S.B. Kang, K.S. Yoon, Y.S. Kwon, Porous TiNi biomaterial by self-propagating high-temperature synthesis, Advanced Engineering Materials 6(6) (2004) 403–406.
[21] A. Biswas, Porous NiTi by thermal explosion mode of SHS: processing, mechanism and generation of single phase microstructure, Acta Materialia 53(5) (2005) 1415–1425.
[22] C. Greiner, S.M. Oppenheimer, D.C. Dunand, High strength, low stiffness, porous NiTi with superelastic properties, Acta Biomater 1(6) (2005) 705–716.
[23] S. Wu, C.Y. Chung, X. Liu, P.K. Chu, J.P.Y. Ho, C.L. Chu, Y.L. Chan, K.W.K. Yeung, W.W. Lu, K.M.C. Cheung, K.D.K. Luk, Pore formation mechanism and characterization of porous NiTi shape memory alloys synthesized by capsule-free hot isostatic pressing, Acta Materialia 55(10) (2007) 3437–3451.
[24] Y.P. Zhang, D.S. Li, X.P. Zhang, Gradient porosity and large pore size NiTi shape memory alloys,

Scripta Materialia 57(11) (2007) 1020–1023.
[25] S. Wisutmethangoon, N. Denmud, L. Sikong, Characteristics and compressive properties of porous NiTi alloy synthesized by SHS technique, Materials Science and Engineering: A 515(1-2) (2009) 93–97.
[26] X.T. Sun, Z.X. Kang, X.L. Zhang, H.J. Jiang, R.F. Guan, X.P. Zhang, A comparative study on the corrosion behavior of porous and dense NiTi shape memory alloys in NaCl solution, Electrochimica Acta 56(18) (2011) 6389–6396.
[27] J. Van Humbeeck, Additive manufacturing of shape memory alloys, Shape Memory and Superelasticity 4(2) (2018) 309-312.
[28] X. Yao, S. Cao, X.P. Zhang, D. Schryvers, Microstructural characterization and transformation behavior of porous $Ni_{50.8}Ti_{49.2}$, Materials Today: Proceedings 2 (2015) S833-S836.
[29] C.B. Ke, X. Ma, X.P. Zhang, Phase field simulation of Ni_4Ti_3 precipitation in porous NiTi shape memory alloys under applied stresses, Materials Science Forum 654-656 (2010) 1504–1507.
[30] S. Cao, W. Tirry, W. Van Den Broek, D. Schryvers, Optimization of a FIB/SEM slice-and-view study of the 3D distribution of Ni_4Ti_3 precipitates in Ni-Ti, Journal of Microscopy 233(1) (2009) 61–68.
[31] S. Cao, W. Tirry, W. Van den Broek, D. Schryvers, 3D Reconstruction of Ni_4Ti_3 Precipitates in a $Ni_{51}Ti_{49}$ Alloy in a FIB/SEM Dual-Beam System, Materials Science Forum 583 (2008) 277–284.
[32] M.W. Phaneuf, FIB for materials science applications - a review, in: L.A. Giannuzzi, F.A. Stevie (Eds.), Introduction to Focused Ion Beams: Instrumentation, Theory, Techniques and Practice, Springer US, Boston, MA, 2005, pp. 143–172.
[33] N. Idowu, C. Nardi, H. Long, T. Varslot, P.-E. Oeren, Effects of Segmentation and Skeletonization Algorithms on Pore Networks and Predicted Multiphase-Transport Properties of Reservoir-Rock Samples, SPE Reservoir Evaluation & Engineering 17(4) (2014) 473–483.
[34] C. Pudney, Distance-Ordered Homotopic Thinning: A skeletonization algorithm for 3D digital images, Computer Vision and Image Understanding 72(3) (1998) 404–413.
[35] W.J. Whitehouse, The quantitative morphology of anisotropic trabecular bone, Journal of Microscopy 101(2) (1974) 153–168.
[36] A. Odgaard, Three-dimensional methods for quantification of cancellous bone architecture, Bone 20(4) (1997) 315–328.
[37] T. Hildebrand, P. Ruegsegger, A new method for the model-independent assessment of thickness in three-dimensional images, J Microsc-Oxford 185 (1997) 67–75.
[38] J. Laeng, Z.M. Xiu, X.X. Xu, X.D. Sun, H.Q. Ru, Y.N. Liu, Phase formation of Ni-Ti via solid state reaction, Physica Scripta T129 (2007) 250–254.
[39] W. Tang, B. Sundman, R. Sandstrom, C. Qiu, New modelling of the B2 phase and its associated martensitic transformation in the Ti-Ni system, Acta Materialia 47(12) (1999) 3457–3468.
[40] K. Gall, K. Juntunen, H.J. Maier, H. Sehitoglu, Y.I. Chumlyakov, Instrumented micro-indentation of NiTi shape-memory alloys, Acta Materialia 49(16) (2001) 3205–3217.
[41] K. Gall, H.J. Maier, Cyclic deformation mechanisms in precipitated NiTi shape memory alloys, Acta Materialia 50(18) (2002) 4643–4657.
[42] W. Tirry, D. Schryvers, Quantitative determination of strain fields around Ni4Ti3 precipitates in NiTi, Acta Materialia 53(4) (2005) 1041–1049.
[43] W. Tirry, D. Schryvers, Linking a completely three-dimensional nanostrain to a structural transformation eigenstrain, Nat Mater 8(9) (2009) 752–757.
[44] D.S. Li, Y.P. Zhang, G. Eggeler, X.P. Zhang, High porosity and high-strength porous NiTi shape memory alloys with controllable pore characteristics, Journal of Alloys and Compounds 470(1–2) (2009)

L1–L5.